Biglobal linear stability analysis of the flow induced by wall injection

F. Chedevergne,[a] G. Casalis,[b] and Th. Féraille[c]
ONERA DMAE, 2 av. Ed. Belin, BP. 4025, 31 055 Toulouse Cedex, France

(Received 19 April 2005; accepted 23 November 2005; published online 12 January 2006)

The hydrodynamic stability of the flow in a solid rocket motor is revisited using a general linear stability approach. A harmonic perturbation is introduced into the linearized Navier-Stokes equations leading to an eigenvalue problem posed as a system of partial differential equations with respect to the spatial coordinates. The system is discretized by a spectral collocation method applied to each spatial coordinate and the eigenvalues are determined using Arnoldi's procedure. A special emphasis is placed on the boundary conditions. The main result is the discrete nature of the eigenvalue set. According to the present theory and the obtained results, only some discrete frequencies may exist in the motor (as eigenmodes). These frequencies only depend on the Reynolds number based on the injection velocity and the radius of the pipe flow. They are compared to measurements that have been performed at ONERA in one case with a cold-gas setup and in another case with a reduced scale live motor. Due to the agreement obtained with both experiments, the biglobal stability approach seems to offer new insight into the unresolved thrust oscillations problem. © *2006 American Institute of Physics*. [DOI: 10.1063/1.2160524]

I. INTRODUCTION

Large solid rocket motors exhibit thrust oscillations under some specific conditions. The amplitude of these oscillations is not very large (maximum 2% or 3% of the mean thrust) and seems to be very sensitive to the environmental conditions; accurate predictions for practical applications are thus not workable up to now. The physical mechanism itself from which the oscillations originate is still not well understood. For about 20 years, several studies have been devoted to this problem. The present paper presents a biglobal approach leading to a model for the theoretical prediction of the observed thrust oscillations.

The published studies can be divided into three groups:

- The first one deals with experimental activities and is itself divided into two subgroups. Experiments with combustion (with the real propellant or a modified one) are on one side, either full scale or using reduced scale motors; so-called "cold-gas" experiments are on the other side. The first ones are obviously more realistic, particularly concerning ambient conditions, such as the pressure, the temperature, the combustion process, and also the slow increase of the cavity volume due to the wall regression. Measurements are not easy in such conditions and only global information is available, usually the steady and the unsteady pressure at the front wall and/or close to the throat. Conversely, setups using gas at ambient conditions work with a constant value of the radius pipe, allow inflow detailed measurements in addition to the ones similar to those used with combustion.
- The second group contains numerical investigations, mainly by using Reynolds-averaged Navier-Stokes solvers. Their main advantage is that this approach allows parametric studies in order to analyze for instance the effects of some cavities, their position, their size, the shape of the nozzle, and the presence of protuberances in the flow.
- The last group includes the theoretical activities that aim to provide physical models for the considered problem. The present paper belongs to it.

Let us start with the current state-of-the-art ideas regarding the thrust oscillations. Experiments with combustion show that these oscillations may appear, but only at some instances of the firing. They also show that the frequency of the oscillations, when they exist, is close to that of one of the longitudinal acoustic modes (the fundamental one or one of its first harmonics). As described in Refs. 1–3, the latter is simply obtained as an irrotational mode by considering the motor as an organ pipe. There is then a rotational contribution due to the flow inside, but it does not modify the frequency itself. However, a detailed analysis of the measurements in the presence of significant pressure oscillations shows that the frequency changes with respect to the time; it exhibits continuous paths (the frequency decreases) and abrupt jumps (sudden increase), moving back the frequency to a value that is close to the acoustic mode (see Fig. 1). This behavior (continuous paths and abrupt jumps) may occur several times in the experiments with combustion either in full scale or in reduced scale. The goal of the different works devoted to this purpose is to understand the physical origin of the oscillations, to be able to predict the associated amplitudes, and finally to propose practical solutions in order to remove them or at least reduce them.

Taking into account the exhibited frequency paths, the acoustic longitudinal mode cannot be the single mechanism. During the firing, the geometry changes as mentioned above; the cavity volume increases due to the increase of the chamber radius where the flow takes place. There are other modi-

[a]Electronic mail: francois.chedevergne@onecert.fr
[b]Electronic mail: gregoire.casalis@onecert.fr
[c]Electronic mail: thierry.feraille@snecma.fr

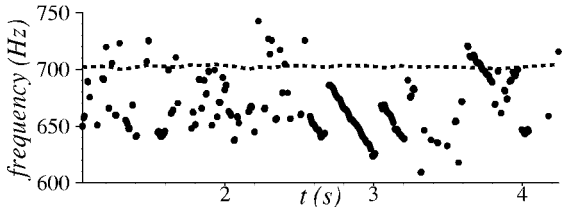

FIG. 1. Time evolution of the frequency of the fluctuation associated to the largest amplitude in symbols. The dashed line represents the frequency evolution of the fundamental cavity mode. The evolution of the latter is due to small variations of the mean quantities. Experiments have been carried out at ONERA with a small scale motor called LP9 (see Ref. 28).

fications that depend on the load structure. As proposed initially by Vuillot,[4] three possible sources of unsteadiness may be invoked: they are called by the acronyms VSA, VSO, and VSP. VSA (angle vortex shedding) may occur at the upper downstream angle of a block of propellant; at this point the wall ejection is not uniform and may induce hence some shear instabilities. VSO (obstacle vortex shedding) is related to the presence of inhibitors between two blocks that appear to be obstacles inside the flow, inducing an unsteady wake. For a long time, VSO has been believed to be either the main source or the only source of the thrust oscillations. However, their role is not so clear as experiments in combustion with metallic (nonabrasive) inhibitors do not present large oscillations whereas the same configuration without inhibitors does present large oscillations, as experimentally proven in Ref. 5. VSP (parietal vortex shedding) does not come from a geometry irregularity but is a hydrodynamic instability of the flow itself, for which a biglobal approach is described in the present paper.

This instability (VSP) cannot be measured directly in experiments with combustion, but it has been identified in different computations,[6] for instance, and in cold-gas experiments. The theoretical approach is based on the usual small perturbation technique: a mean (or basic) flow being given (the so-called Taylor flow in the present case as it will be reminded in the following), a perturbation is superimposed without any forcing term in the boundary conditions (the perturbation is assumed to be an eigenmode). Then due to the linearization and to some symmetries of the mean flow, a particular mathematical form for the perturbation is prescribed, leading usually to an ordinary differential equation with respect to the coordinate associated with the normal distance from the injection wall. The first investigations consider the plane geometry and the pioneers are Varapaev and Yagodkin.[7] As discussed in Ref. 8, their approach is not fully consistent by assuming for the perturbation an exponential dependence with respect to the streamwise coordinate and by keeping at the same time the nonparallel terms induced by the mean flow. However, using the same theoretical approach and again for the plane geometry, the first validation with respect to cold-gas experiments is given in Ref. 9. It is proved that even if not fully coherent the nonconsistent quasiparallel approach gives results that are in very good agreement with the measurements. A first extension to the cylindrical and more realistic geometry is given in Ref. 10 with a similar approximation for the nonparallel terms. Some general comparisons with experimental results are published in Ref. 11. However, in both cases, if the agreement between the measurements and the theoretical results seems to be acceptable, some noticeable differences remain that do not seem to exist in the plane case.

The most probable weakness of the theoretical stability approach used is in relation to the nonparallel effects and consequently to the induced inconsistency. According to the theory used, the critical frequency (the one that crosses first the neutral curve) is about twice as large in the cylindrical geometry compared to the plane case. This leads to a wavelength that is about half its value in the plane case. Thus, one can explain why the nonparallel effects can be more important in the cylindrical case than in the plane configuration. To solve this difficulty the present biglobal approach treats the mean flow as a general function of two spatial coordinates (x and r in the present case). This approach is more general but needs more computational resources than the classical stability theory. Due to the improvement of the computational capacities (the random-access memory and not the speed in our case), the general approach starts to be used for different mean flows. The first application was the laminar Poiseuille flow that may exist in a rectangular duct (see Ref. 12). This configuration has the advantage to be mathematically well posed with respect to the boundary conditions, therefore, it plays the role of a test case for code validation. The stability analysis for this flow has been revisited successfully (see Ref. 13 and later in Refs. 14 and 15). Then the laminar boundary layer on an infinite swept wing in the neighborhood of the attachment line has been investigated by some contributors (see Refs. 13 and 16). Other flow configurations have been analyzed using this technique such as a separation bubble in a boundary layer.[17] In these configurations, at least one of the boundaries is not a physical one and thus "ad hoc" conditions must be imposed on it (see Refs. 16 and 18) as it is also routinely done for Navier-Stokes computations with exit boundary conditions.

We also developed a code to be applied to strongly nonparallel flows and validated it (see Ref. 19) in comparison with previous studies.[16,18] The present flow induced by wall injection, however, has not been investigated previously by the general approach; to our knowledge, this is the first contribution.

The present paper starts with a description of the physical model including the geometry, the mean flow under investigation, and a short summary of the standard linear stability approach, which is not consistent in the present case as explained above. Then, a short description of two experimental setups is given, one with cold gas, the other with a small scale solid propellant motor. Finally, the biglobal approach is detailed, first with the governing equations and boundary conditions, then with the numerical procedure. A special emphasis is made on the nonphysical boundary exhibited in the present configuration. Finally numerical results are given in comparison with the experimental ones.

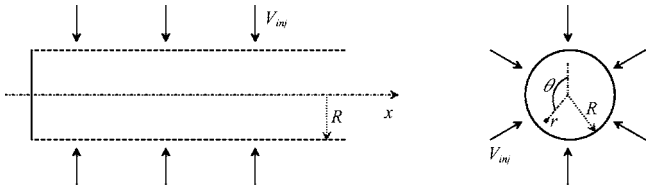

FIG. 2. Cylindrical coordinate system (r,θ,x). Flow is injected through the cylindrical wall located at $r=R$ with the injection velocity V_{inj}. The pipe is bounded by a solid wall located at $x=0$.

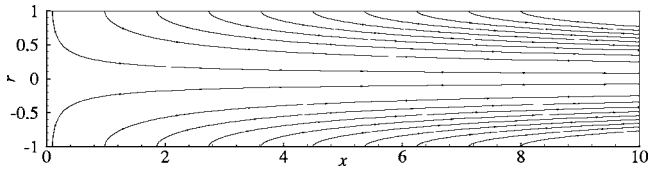

FIG. 3. Some streamlines corresponding to the Taylor-Culick basic flow (3).

II. PHYSICAL MODEL

The description given below corresponds directly to the flow existing in a cold-gas setup. The application to a live motor is explained in the last part of this section.

A. Geometry

The configuration considered is a cylindrical pipe; the base is circular of radius R. The coordinate system is the usual cylindrical one (r,θ,x) as indicated in Fig. 2. The pipe is limited by a hermetic front wall located at $x=0$ and is supposed to be very long in the direction of positive values of x. Through the cylindrical wall, flow is injected and it is assumed that the injection velocity denoted by V_{inj} is uniform (independent of x and θ), constant (independent of the time t), and normal to the wall. In some conditions, e.g., in live motors, the radius and the injection velocity vary with respect to time, but due to the different involved time scales, both quantities can be confidently assumed to be constant, see Sec. II E 3 for more details.

B. Governing equations

The flow is assumed to be an incompressible viscous fluid, so that the dimensionless velocity vector $\underline{U}=(U_r,U_\theta,U_x)$ and the dimensionless pressure P satisfy the standard Navier-Stokes equations

$$\begin{aligned}&\underline{\nabla}\cdot\underline{U}=0\\&\frac{\partial\underline{U}}{\partial t}+\underline{\underline{\nabla U}}\cdot\underline{U}+\underline{\nabla P}=\frac{1}{\mathcal{R}e}\Delta\underline{U}.\end{aligned}\tag{1}$$

In these equations the distances, the velocity components, the time and the pressure have been made dimensionless thanks to, respectively, the radius R, the wall injection velocity V_{inj}, R/V_{inj}, and ρV_{inj}^2, where ρ is the flow density that is assumed to be constant. It remains the Reynolds number $\mathcal{R}e$ based on the injection velocity and the radius R. Associated with this system (1), the following boundary conditions are imposed:

$$\begin{aligned}&\forall x,\theta,t\quad U_r(R,\theta,x,t)=-1\quad U_\theta(R,\theta,x,t)=U_x(R,\theta,x,t)=0\,,\\&\forall r,\theta,t\quad U_r(r,\theta,0,t)=U_\theta(r,\theta,0,t)=U_x(r,\theta,0,t)=0\,,\\&\forall x,\theta,t\quad \|\underline{U}(0,\theta,x,t)\|,|P(0,\theta,x,t)|\text{bounded}\,,\end{aligned}\tag{2}$$

expressing the uniform normal injection, the no-slip condition at the front wall, and the regular behavior at the axis $r=0$ where the cylindrical coordinate system is ill posed.

C. Mean flow

The previous system (1)+(2) is used for the stability problem. Concerning the mean flow, there are three main types of solution depending on possible approximations of Eqs. (1) and of the boundary conditions (2):

- (1)+(2): only CFD solutions can be found, as far as the authors know.
- (1)+(2) without the no-slip condition at the head end $x=0$: a self-similar solution has been found by Berman.[20]
- (1) inviscid (Euler equations)+(2) without the no-slip condition at the head end $x=0$: an exact (self-similar) analytical solution exists,

$$\left.\begin{aligned}U_r^{(b)}&=-\frac{1}{r}\sin\frac{\pi r^2}{2}\\U_x^{(b)}&=\pi x\cos\frac{\pi r^2}{2}\end{aligned}\right\}\quad P^{(b)}=-\frac{\pi^2x^2}{2}-\frac{1}{2r^2}\sin^2\left(\frac{\pi r^2}{2}\right)+P_0,\tag{3}$$

with P_0 a constant. It is the so-called "Taylor" flow. Some streamlines associated with the Taylor flow (3) are plotted in Fig. 3. As expected, the streamlines come from the wall. The figure also shows that for large values of x, the streamlines become more or less parallel. In a region very close to the wall, however, the flow is strongly nonparallel.

In Ref. 10, comparisons between the last two solutions show that they are nearly identical for $\mathcal{R}e$, typically greater than 1000. The classical stability approach applied to these two solutions leads of course to the same observation. Table I provides numerical values obtained by the biglobal approach (see Sec. III) for a small Reynolds number using the last two solutions of the mean flow. It clearly shows that the choice of the mean flow weakly affects the stability results. The higher the Reynolds number is, the lower the difference is. In practice, the results are computed for $\mathcal{R}e$ of greater than 1000 so that the effect is considered to be negligible.

Concerning the first type of solution (CFD), numerical results obtained by Lupoglazov and Vuillot in Ref. 6 and by others show that, except in a region very close to the head end, the mean flow coincides with the other solutions (for $\mathcal{R}e\geqslant 1000$). Actually, close to the head end, the problem is not completely solved (as discussed in a private communication with Vuillot). Consequently, only the two self-similar solutions can be confidently used for biglobal stability analysis.

TABLE I. Comparison between stability modes computed with the viscous and the inviscid self-similar mean flow.

	$\mathcal{R}_e=100$		$\mathcal{R}_e=500$		$\mathcal{R}_e=1000$	
	Inviscid	Viscous	Inviscid	Viscous	Inviscid	Viscous
Mode 1	$7.059-6.792i$	$7.114-6.812i$	$5.912-5.333i$	$5.921-5.340i$	$5.478-4.931i$	$5.482-4.934i$
Mode 2	$12.547-9.726i$	$12.607-9.723i$	$10.892-7.485i$	$10.906-7.488i$	$10.189-6.813i$	$10.196-6.815i$
Mode 3	$17.083-12.419i$	$17.134-12.421i$	$15.224-9.451i$	$15.240-9.453i$	$14.378-8.549i$	$14.386-8.551i$
Mode 4	$21.114-14.854i$	$21.140-14.871i$	$19.060-11.331i$	$19.075-11.336i$	$18.130-10.258i$	$18.139-10.261i$

D. Classical linear stability theory

Based on the small perturbation technique, the standard linear stability theory is now widespread in several fluid mechanics configurations; see Ref. 21 for a recent and detailed review. More specifically, the case of the flow induced by wall injection (or suction) has been investigated both for small Reynolds numbers in Refs. 22 and 23 and for large Reynolds numbers (the present case); see Ref. 24 for a review. The principle is to assume that the actual flow consists in the superposition of the considered basic flow, given by (3) and identified by the superscript (b) and of an unknown perturbation. This is imposed by

$$\underline{U}=\underline{U}^{(b)}+\underline{u}, \quad P=P^{(b)}+p, \tag{4}$$

with $\underline{u}$ and p the velocity field and the pressure of the perturbation, being *a priori* general functions of (r,θ,x,t). In the linear approach the amplitudes of $\underline{u}$ and p are supposed to be very small in comparison with the ones of $\underline{U}^{(b)}$ and $P^{(b)}$. The superposition is introduced in the governing system (1)+(2) and, with the linear assumption, nonlinear terms with respect to perturbation quantities are neglected. The following systems are then obtained:

$$\begin{aligned} &\underline{\nabla}\cdot\underline{u}=0 \\ &\frac{\partial \underline{u}}{\partial t}+\underline{\underline{\nabla U^{(b)}}}\cdot\underline{u}+\underline{\underline{\nabla u}}\cdot\underline{U}^{(b)}+\underline{\nabla p}=\frac{1}{\mathcal{R}e}\Delta\underline{u}, \end{aligned} \tag{5a}$$

$$\begin{aligned} &\forall x,\theta,t \quad \underline{u}(R,\theta,x,t)=0 \\ &\forall r,\theta,t \quad \underline{u}(r,\theta,0,t)=0 \\ &\forall x,\theta,t \quad \|\underline{u}(0,\theta,x,t)\|,|p(0,\theta,x,t)|\text{bounded}. \end{aligned} \tag{5b}$$

The zero perturbation is of course a solution. However, in many cases, a nonzero solution exists; it is called an eigenmode. Roughly speaking, if the latter increases with respect to time (it is assumed to have a very small amplitude at the beginning in order to allow the linear treatment) the basic flow is claimed linearly unstable whereas conversely if it decreases the basic flow is claimed to be linearly stable. Usually in practice, only some of the eigenmodes are amplified thus determining "dangerous" frequencies, wavelengths, or other parameters related to the amplified eigenmodes.

Then, influenced by the mean flow velocity, which acts as coefficient in the linear system (5a), the mathematical form of the perturbation is prescribed. The approach proposed in the present article is actually, to the best of our knowledge, new for the Taylor flow with respect to this form (see Sec. III).

The classical theory assumes that the mean flow is quasiparallel. This leads to the nonconsistent approach with the usual normal mode form for any fluctuating quantity q:

$$q=\tilde{q}(r)e^{i(kx+m\theta-\omega t)}, \quad \omega=\omega_r+i\omega_i, \tag{6}$$

with m an integer, k a real number (in the framework of the temporal theory), and ω a complex number, its real part corresponding to the circular frequency and its imaginary part to the temporal growth rate. The amplitude function $\tilde{q}$ is a function of r only. Introducing this particular normal mode form into (5a) leads to a system of ordinary differential equations (ODEs) with respect to r. The boundary conditions (5b) are written in terms of the amplitude functions, except for the no-slip condition at the head end, which cannot be satisfied.

As shown in Ref. 9, this approach is in very good agreement with the measurements performed in a cold-gas setup in the case of a duct with a rectangular section and for not too small distances from the head end ($x=0$). The main result is a range of frequencies that are highly (actually exponentially) amplified with respect to x. Concerning the more relevant axisymmetric configuration, the agreement is not very good with the experimental results (see Ref. 10).

The shortcomings of this classical approach are as follows:

- it is not consistent;
- it can be applied only for large values of x independently of what happens for other values of x and consequently the boundary condition at $x=0$ in (5b) cannot be satisfied;
- it is less suitable in axisymmetric configurations than in planar cases.

In order to overcome these difficulties, a biglobal stability approach (consistent) is proposed and will be detailed in Sec. III. The remaining part of the present section is devoted to the description of two different experimental setups for the subsequent comparisons that will be done at the end of the present paper.

E. Experimental setups

1. The VALDO cold-gas facility

Experimental investigations have been carried out using the so-called VECLA setup for which the section is rectangular; some results can be found in Ref. 9. VALDO is based on the same principle: cold gas is injected through a porous wall, but has a circular section, which is more realistic for

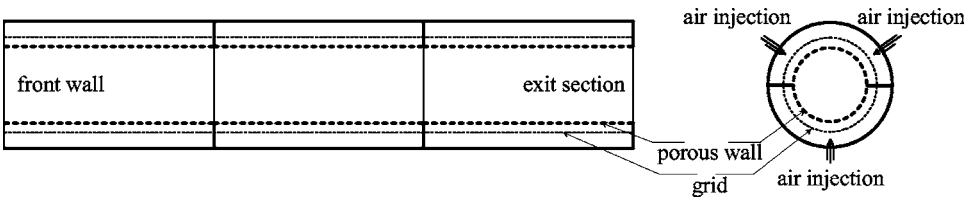

FIG. 4. Schematic view of the VALDO setup. Air is injected in the three (two, three, or four) elements; a grid aims to spread out the injected air. Finally air is injected in the cavity through a poral.

comparisons with real solid rocket motors. Similar setups have been previously used (see Refs. 11 and 25 or Ref. 26).

VALDO is located at ONERA in Palaiseau; the experiments are carried out by G. Avalon. A detailed description of the setup may be found in Ref. 27; only the main characteristics are given below. There are four identical elements (only one is equipped with a pressure probe and a hot wire), the length of each being 168 mm and the inside diameter 60 mm. VALDO may operate with two, three, or four elements, leading to a total length of 336, 504, or 672 mm. The structure of the interior wall is a poral (porosity 2 μm in the present case). Air is injected at three different azimuthal angles for each element used and is assumed to be spread out uniformly with respect to the axial direction and the azimuthal one thanks to a grid placed between the external structure and the poral (see Fig. 4). Finally the air is injected inside the cavity at the injection velocity V_{inj} with a direction assumed to be normal to the wall and with a norm assumed to be constant in space.

The exit section can be either free (air goes directly in the atmosphere) or equipped with a (sonic) throat. The injection velocity can be varied directly in the first case and in the second case by a needle, placed in the middle of the throat, which has a varying section and which can be moved more or less in the axial direction. Changing the critical section forces a change of the mass flow rate and thus of the injection velocity. Typical values of the injection velocity and the corresponding Reynolds number $\mathcal{R}e$ are given in Table II.

In this cold-gas facility, direct measurements in the flow are possible; they are performed with a hot wire. When a throat is mounted at the exit section, only very few positions in x are available for this measurement, each one corresponding to one position of the equipped element. When the exit section is free, a long shaft, carrying the hot wire probe, is introduced through the exit and may be moved all along the pipe. In addition, the instantaneous pressure is measured at the front wall and close to the exit section. The data acquisition is done during 1 s at a rate of 4000 points per second. The signal is then filtered between 50 Hz and 2000 Hz. Finally a spectral analysis is performed using the spectrogram method applied to the 2048 first points of each acquisition. This procedure leads to the FFT of the fluctuating velocity and pressure, as it will be presented below.

TABLE II. Typical operating conditions using VALDO, air is at ambient conditions so that the kinematic viscosity is about $\nu=15\times10^{-6}$ m^2 s^{-1}. The radius of the pipe is $R=30$ mm.

Free exit section	With a throat
$V_{\text{inj}}=0.84$ ms^{-1}, $\mathcal{R}_e=1680$	$V_{\text{inj}}=0.55$ ms^{-1}, $\mathcal{R}_e=1100$
$V_{\text{inj}}=1.05$ ms^{-1}, $\mathcal{R}_e=2100$	

2. The reduced scale solid rocket motors LP9

As explained in Sec. I, several sources are mentioned as being responsible for the thrust oscillations observed in large solid rocket motors. In order to prove the key role played by the hydrodynamic instability considered in the present paper, simple motors have been investigated for some years at ONERA Le Fauga-Mauzac centre by M. Prévost and his colleagues (see Ref. 28). Numerous configurations have been investigated. In this paper only the so-called LP9-15 will be analyzed. It corresponds to a very simplified geometry of the European launcher Ariane 5 boosters, the scale being 1/35. A schematic view is given in Fig. 5. In this configuration, there is a free cavity upstream close to the front wall and there are two cylindrical blocks of propellant. There is no cavity in the vicinity of the nozzle at the exit. On the other hand, there is a small cavity between the two blocks and it must be noted that a varnish is put on the lateral surfaces of the propellant block so that it may be expected that combustion does not occur on this lateral surface. The combustion generates a flow with a small injection velocity normal to the wall (close to 1 m/s). The velocity components of the mean flow are very close to the ones given in (3), as demonstrated by different numerical simulations; see, e.g., Refs. 4 and 29. In addition, these computations show that, except in a zone very close to the propellant surface, the pressure and the temperature in the cavity are roughly uniform. This explains why there is no real coupling between the dynamics and the energy equation. The effects of laminar premixed flame oscillations are limited to a thin region above the burning surface as shown in Refs. 30 and 31. The flow velocity is very close to the incompressible solution and the stability analysis can also be performed using the incompressible approximation.

At the beginning of the firing, the radius of the cavity is 20 mm; at the end, which occurs 4 s later, the radius is 42.5 mm.

3. About the unsteady effects

Two types of experiments have been performed: one cold-gas set up (VALDO) with a fixed geometry and a small scale solid propellant motor (LP9). As explained above, the first setup has been used either in static conditions (fixed injection velocity) or in dynamic conditions (variable injec-

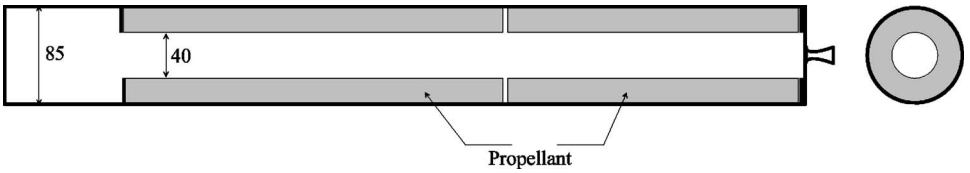

FIG. 5. Schematic view of the LP9 setup for the firing 15. The sizes are in mm.

tion velocity), whereas the geometry in a live motor is necessarily unsteady (decrease of the propellant quantity inside the cavity). From a theoretical point of view an exponential dependence in $\exp(-i\omega t)$ for the perturbation in a linear approach is justified in static conditions, when the geometry and the mean flow are really steady.

Concerning the dynamic experiments, this exponential dependence may appear questionable. In fact, as it has been shown in Ref. 32, the time scale that is associated with the increase of the geometry in a live motor (small scale and full scale) is larger than the time scale associated with the first longitudinal acoustic mode (small scale motor). As mentioned above, 4 s corresponds to an increase of nearly 20 mm, so that a 1% increase of the geometry needs 0.04 s, which is significantly larger than the 1/700 s associated with the time scale of the acoustic mode (see Fig. 1). The same is true for the injection velocity variation in VALDO. The increase of the injection velocity from 0.6 to 2 m/s is performed in about 30 s. Thus, a 1% increase of the injection velocity takes 0.43 s, which is very slow compared to the characteristic time (1/400 s) of the main phenomenon (detailed in Sec. III D; see Fig. 12).

Thus, in terms of a regular WKB approach, the exponential dependence for the fluctuation corresponds to the leading order terms. In Ref. 32 one additional term has been calculated (in the framework of the nonconsistent approach), whose influence can be confidently neglected. In the following the basic flow will be considered as steady even for the (weakly) unsteady experiments.

III. BIGLOBAL STABILITY ANALYSIS

A. Eigenvalue problem

The goal of this section is to describe the biglobal approach used to solve the problem composed by the linearized Navier-Stokes (LNS) system (5a) and by the boundary conditions (5b).

1. Differential equations

As explained above (see Fig. 3), the Taylor flow is nonparallel. The idea of the proposed biglobal stability approach is to perform an analysis that is as general as possible for a fully nonparallel basic flow. As the coefficients of the LNS system do not depend on t and θ, any perturbation $q=(u_r,u_\theta,u_x,p)$ can be searched with the following form:

$$q=\hat{q}(x,r)e^{i(m\theta-\omega t)}m\in\mathbb{N},\omega\in\mathbb{C}, \tag{7}$$

where m stands for the azimuthal wave number. The real part ω_r of ω is the dimensionless circular frequency and the imaginary part ω_i is the temporal growth rate. The classical approach (6) has an explicit x dependence (in relation with the parallel assumption), whereas the proposed one does not assume anything for the x dependence.

This study is limited to the axisymmetric modes given by $m=0$ and so, in the following, one mode will be completely identified by the complex number ω. If $m=0$, and so $\hat{u}_\theta=0$, a streamfunction can be defined such that

$$\hat{u}_x=\frac{1}{r}\frac{\partial\hat{\phi}}{\partial r},\quad \hat{u}_r=-\frac{1}{r}\frac{\partial\hat{\phi}}{\partial x}. \tag{8}$$

Then the LNS system (5a) leads for the differential equations to a scalar equation written for the streamfunction:

$$\frac{1}{r}\frac{\partial\Psi}{\partial r}\frac{\partial\left(\mathcal{L}\hat{\phi}\right)}{\partial x}-r\frac{\partial\Psi}{\partial x}\frac{\partial}{\partial r}\left(\frac{1}{r^2}\mathcal{L}\hat{\phi}\right)+\frac{\partial\hat{\phi}}{\partial r}\frac{\partial}{\partial r}\left[\frac{1}{r}\frac{\partial}{\partial r}\left(\frac{\partial\Psi}{\partial x}\right)\right]-r\frac{\partial\hat{\phi}}{\partial x}\frac{\partial}{\partial r}\left[\frac{1}{r}\frac{\partial}{\partial r}\left(\frac{1}{r}\frac{\partial\Psi}{\partial r}\right)\right]-\frac{1}{Re}\mathcal{L}\left(\mathcal{L}\hat{\phi}\right)=i\omega\mathcal{L}\hat{\phi}, \tag{9}$$

where

$$\mathcal{L}=\frac{\partial}{\partial x^2}+\frac{\partial}{\partial r^2}-\frac{1}{r}\frac{\partial}{\partial r}$$

is a linear operator and Ψ is a streamfunction of the mean flow. Relation (9) is a partial differential equation (PDE) of order four in r and x and must be solved in a domain Ω in the (x,r) plane. The chosen domain is $\Omega=[0,X_e]\times[0,1]$, where X_e stands for an artificial exit section. This equation leads to an elliptic problem and will be associated with boundary conditions on all the boundaries.

2. Boundary conditions

On the front wall $x=0$ and on the porous wall $r=1$, the no-slip conditions written in (5b) are imposed. Using (8), the conditions are

$$\frac{\partial\hat{\phi}}{\partial x}(0,r)=0,\quad \hat{\phi}(0,r)=0;\quad \frac{\partial\hat{\phi}}{\partial r}(x,1)=0,\quad \hat{\phi}(x,1)=0, \tag{10}$$

choosing an integration constant equal to zero. There are different ways to impose the last boundary condition of (5b) on the axis $r=0$. First, one can use a Taylor series expansion of about zero. Second, given the symmetry of the problem, one can show that $\hat{\phi}$ has to be an even function with respect to r that vanishes on the axis. The two approaches are equivalent and lead finally to

$$\hat{\phi}(x,0)=0, \quad \frac{\partial\hat{\phi}}{\partial r}(x,0)=0, \quad \frac{\partial^3\hat{\phi}}{\partial r^3}(x,0)=0. \tag{11}$$

It remains a condition to be imposed at the exit $x=X_e$. The chosen exit condition is simply a linear extrapolation in the streamwise direction x. If N_x is the number of points used to discretize the domain Ω in the streamwise direction (e.g., $X_{N_x}=X_e$) then the condition can be written as

$$\forall r\,\hat{\phi}(X_{N_x},r)=\frac{X_{N_x}-X_{N_x-2}}{X_{N_x-1}-X_{N_x-2}}\hat{\phi}(X_{N_x-1},r) + \frac{X_{N_x-1}-X_{N_x}}{X_{N_x-1}-X_{N_x-2}}\hat{\phi}(X_{N_x-2},r). \tag{12}$$

In Sec. III B some comments are given about the validity of such a condition.

Once the problem is well posed, a spectral collocation method (see Ref. 33) based on the Chebyschev polynomials is used to solve numerically the problem (9)+(10)+(11)+(12). Each function of $(\hat{u}_r,\hat{u}_\theta,\hat{u}_x,\hat{p})$ is decomposed on the base of the Chebyschev polynomials for the two variables x and r. So the linear system can be written as an algebraic system defining a generalized eigenvalue problem:

$$\underline{\underline{\mathcal{A}}}\,\underline{\hat{\phi}}=\omega\underline{\underline{\mathcal{B}}}\,\underline{\hat{\phi}}, \tag{13}$$

where $\underline{\hat{\phi}}$ represents an arrangement of the discretized points of the streamfunction $\hat{\phi}$. Now, the difficulty consists in finding the eigenvalues and eigenvectors of (13). In spite of the spectral accuracy, which allows to use only a low number of points in the domain, the matrices size remains large to ensure the convergence (basically, of the order of $10\,000\times10\,000$). It is not possible to get the entire spectrum of (13), and so the well-known Arnoldi procedure[34] (where the size of Krylov subspaces is equal to 200) is used, providing only a few eigenvalues around a given target. The last step consists in identifying the physical eigenvalues among those coming from the computation and further focusing on the most amplified ones (largest values of ω_i). Fortunately, the interesting eigenvalues seem to be isolated from the others.

B. Some comments on the questionable boundary conditions

Some boundary conditions are questionable: the exit condition, the head end boundary condition, and the choice of the integration constant for $\hat{\phi}$.

There is no physical condition that can be imposed in $x=X_e$. Nevertheless, choosing an appropriate exit condition is crucial to make the calculation feasible and relevant. It is expected that for a sufficiently long domain Ω, the eigenvalues and the corresponding eigenfunctions are independent of the value of X_e and of the condition imposed at this exit section.

Many kinds of conditions have been tried, but just a few of them fulfill the previous requirement. For instance, a buffer domain has been added where the elliptic original problem has been turned into a parabolic one. This technique leads to unsatisfying results. Another failure arises by forcing an exponential x dependence as defined in the classical stability approach (6). The tried condition is $(\partial\hat{\phi}/\partial x)-ikX_e\hat{\phi}=0$, with k the wave number computed for the abscissa X_e and for a given complex number ω.

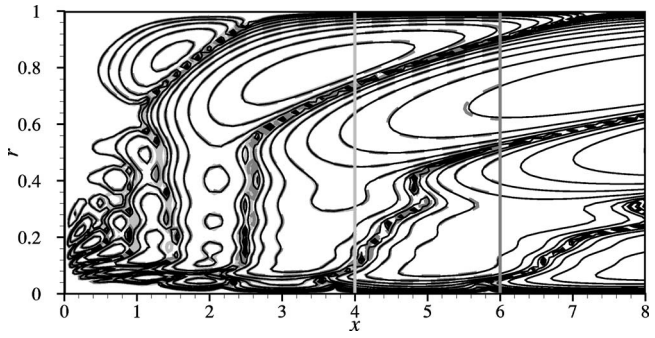

FIG. 6. Contours of $|\hat{\phi}_r|$ for the mode $\omega_r=20.83$, $\mathcal{R}e=2100$, and for three calculations: $X_e=4$, 6, and 8. $X_e=4$ corresponds to the (colored) thick lines, $X_e=6$ to the dashed lines, and $X_e=8$ to the thin lines. In order to see the different details, the aspect ratio is not respected.

Up to now, the only kind of condition that gives satisfactory results is the polynomial extrapolation, and particularly, the linear extrapolation written in (12). Previously, this condition has been successfully applied for nonparallel flows; see the pioneering study by Lin and Malik[16] and by Theofilis[35] for a recent and complete review on these flows. In the present case with this condition, the results are independent of the value of X_e as long as the eigenfunctions are decaying in the streamwise direction or are slowly growing. This arises for the first modes ω_r lower than about 25 (depending on the Reynolds number $\mathcal{R}e$; here $\mathcal{R}e=2100$). Let us give an example. Three values of X_e have been tested : 4, 6, and 8 for a Reynolds number equal to 2100, for 120 points in x and 120 in r. The eigenvalue $\omega_r=20.83$ has been found to be independent of X_e. Furthermore, looking at the absolute value of the real part of the corresponding streamfunction $|\hat{\phi}_r|$ (see Fig. 6), it seems that the different contours are superimposed, except in a region very close to the chosen exit. For large values of ω_r, as the problem is elliptic and as the eigenfunctions are exponentially growing with respect to X, the linear extrapolation modifies the eigenfunction in the neighborhood of X_e. The longitudinal growth is only locally changed around the exit X_e due to the linear extrapolation. Consequently, the eigenvalues ω are weakly affected. This nonzero dependence is not observed in the swept attachment line case; see Refs. 16 and 35. However, in this case, the streamwise growth is polynomial. The local modification of the longitudinal growth due to the linear extrapolation is weaker than in the present case where the amplification is exponential. Finally, the modifications on the values of ω are sufficiently weak to be confident with the independence of the truncated domain length. (A 40% increase of X_e makes ω_r decrease by less than 1%.) Thus, due to the observed independence of the artificial boundary condition, relation (12) has been used for all the following results.

The second point concerns the head end boundary condition. This problem has two different aspects that deal with the main flow and with the calculated perturbation itself. The

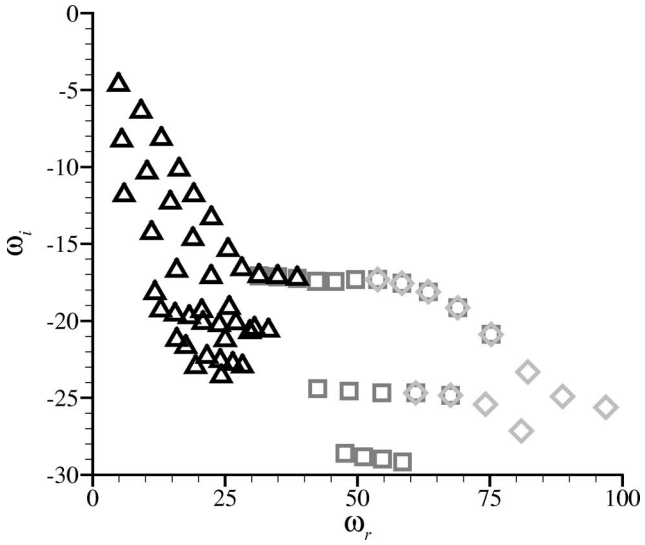

FIG. 7. Eigenvalue spectrum for $\mathcal{R}e=2100$, $Xe=4$, and three different targets. All the eigenvalues obtained with a given target are represented by the same symbol. There is a perfect overlapping between the three computations.

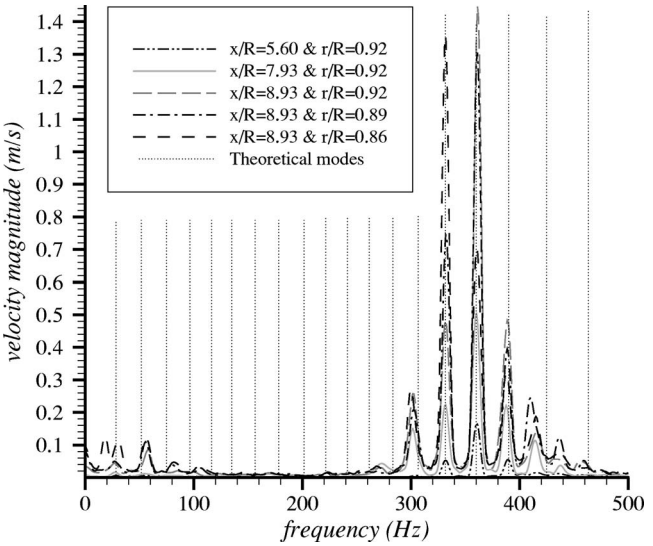

FIG. 8. Comparison between the measured frequencies in VALDO corresponding to five different positions of the hot wire and the dimensionalized theoretical modes.

first aspect has been previously discussed (see Sec. II C). More details are, however, given below. The two self-similar solutions do not satisfy the no-slip condition at $x=0$ (the radial velocity component is not zero) whereas it does at the injection wall. CFD laminar Navier-Stokes calculations[36] show that the Taylor profile is recovered in a region very close to the head end (which depends on the Reynolds number; $x=0.1$ for practical applications). As the mean flow components are the coefficients of the system (5a), only a few matrix coefficients of $\underline{\underline{\mathcal{A}}}$ would be weakly changed if the no-slip condition at $x=0$ was taken into account in the mean flow. Thus, the eigenvalues and the corresponding eigenfunctions can be assumed to be slightly affected by this choice of mean flow.

Now that the Taylor solution is chosen to be the mean flow, it could be interesting to look at a perturbation that satisfies the same set of boundary conditions, in particular, a perturbation that is symmetric with respect to x as is the Taylor flow. In that case the problem can be solved with two different approaches (see Appendix): using an ODE-based approach or the biglobal approach described above. The results are the same. This validates our biglobal stability code. However, modifying a boundary condition for the perturbation makes the problem completely different. The obtained solutions are not observed in the experiments, and it can be concluded that the no-slip condition at the head end for the perturbation is a crucial condition.

Finally, it appears that the no-slip condition at the head end plays a major role for the computation of the stability results only because of its effect on the calculated perturbation but (probably) not because of its effect on the mean flow.

Another questionable point related to the boundary conditions is the condition $\hat{\phi}=0$ on the walls. Actually $\hat{\phi}$ could be any constant $\hat{\phi}_0$ on the walls. Nevertheless, our numerical procedure is more efficient by choosing $\hat{\phi}_0=0$. However, another formulation has been introduced. It consists in writing the system with two variables $U=\partial\hat{\phi}/\partial r$ and $V=\partial\hat{\phi}/\partial x$ satisfying Eq. (9) and a coupling equation that is just the commutativity of the partial derivatives with respect to r and x. This second system gives the same results as the previous formulation. Therefore, in the following the formulation used to perform the calculations will not be mentioned.

C. Results

In the following comparisons with the experimental results, the computed circular frequencies ω_r will be turned into dimensionalized frequencies using the formula

$$f=\frac{V_{\text{inj}}}{2\pi R}\omega_r. \tag{14}$$

There is thus a linear relationship between f and ω_r with a coefficient equal to $V_{\text{inj}}/2\pi R$.

This section is divided into two parts, whether V_{inj} and R are fixed in time or not. First, static results will be explored and compared to the measurements issued from the VALDO facility. They correspond to a constant coefficient in the previous relationship (14). Conversely, associated with a variable coefficient, a dynamic study will be performed using the different experimental results coming from VALDO and LP9 setups.

1. Static results

The results (eigenvalues and eigenfunctions) depend on the value of the Reynolds number $\mathcal{R}e$ only. This Reynolds number $\mathcal{R}e$ is based on the radius R and the velocity injection V_{inj}. Thus, $\mathcal{R}e$ is a constant and the whole set of eigenvalues, called a spectrum, is fixed. A typical spectrum, obtained for $\mathcal{R}e=2100$, is shown in Fig. 7 in the (ω_r,ω_i) plane. It has been obtained with three different targets in the Arnoldi procedure. There are two remarkable points for this spectrum.

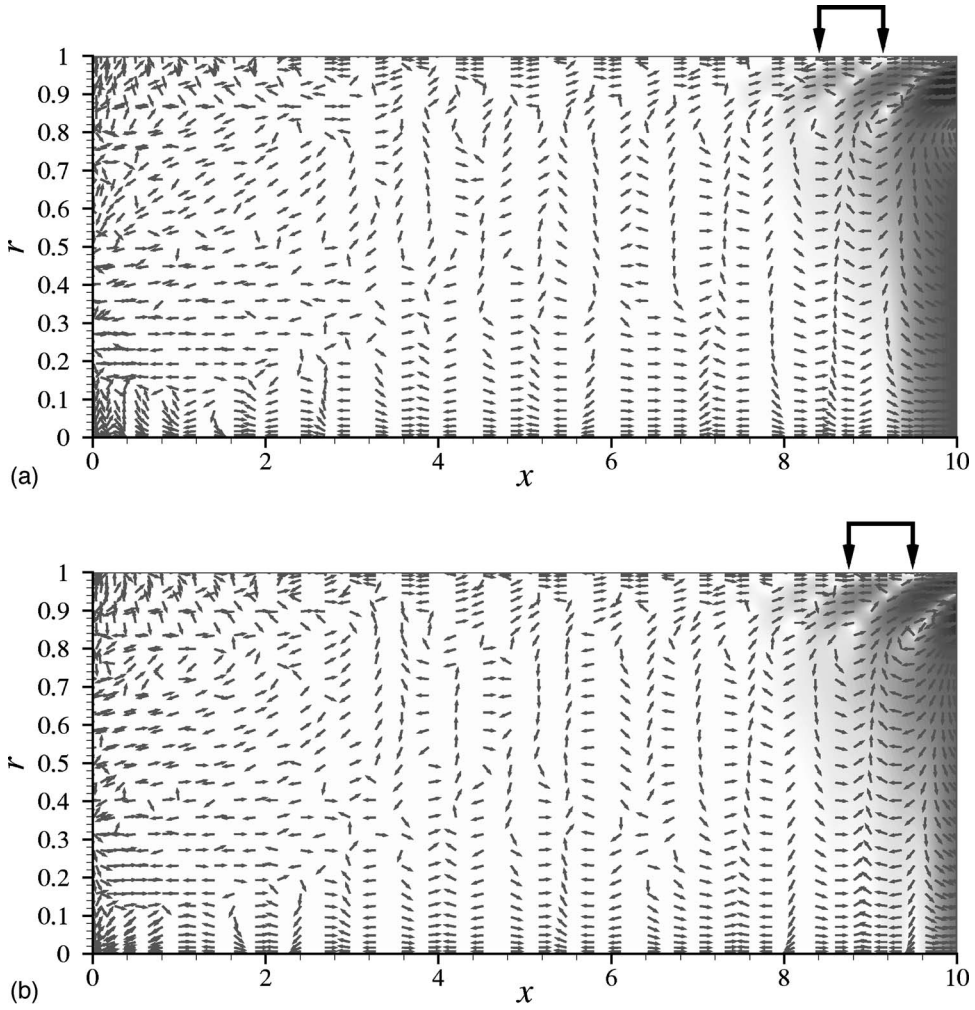

FIG. 9. Velocity field and rms velocity filled contours of the eigenfunction associated to the mode $\omega_r=63.576$ ($f=360$ Hz) computed for $X_e=10$ and $\mathcal{R}e=2100$.

First, the spectrum exhibits discrete eigenvalues (at least for the most amplified ones). Thus, according to the present biglobal approach only a discrete set of values of the circular frequency ω_r of the perturbation can be expected in the considered flow. This is a strong difference between the biglobal approach (which will be referred to as 2D) and the classical monodimensional theory (referred to as 1D) that exhibits a continuous spectrum. It also implies that the frequency signature of the perturbation remains the same in any spatial location (x,r) of the domain Ω.

Figure 8 shows a FFT transform of five measured rms velocity signals. Each of them comes from a different spatial location (x,r) of the hot wire. As indicated in the legend, three values of x at a given radial position r and three values of r at a given distance x are considered. In addition to these five experimental results, the discrete calculated frequencies are indicated by vertical dashed lines. For this comparison, the injection velocity is $V_{\text{inj}}=1.05$ m/s, which yields the Reynolds number $\mathcal{R}e=2100$ (the radius is 30 mm) used for the stability computation. This figure shows first that the measured frequencies are organized as discrete thick peaks that are independent of x and r. Furthermore, these peaks belong to the set of the 2D modes, and the matching is very satisfactory. The pressure measured at the front wall and at the exit section exhibits exactly the same peaks. With this 2D approach, it is thus now possible to predict the set of frequencies that can develop in the Taylor flow.

Second, all the eigenvalues have a negative imaginary part ω_i, which means that all the associated modes are temporally stable. However, some of the associated eigenfunctions are spatially growing. In particular, for $\mathcal{R}_e=2100$ and ω_r of greater than 25, all the eigenfunctions are exponentially growing in the streamwise direction x. For one mode, there are two opposite effects. On one hand, the perturbation amplitude is decreasing when time goes on. On the other hand, there is an exponential growth in the streamwise direction. However, due to the temporal damping, a continuous external excitation must exist to explain the existing measured peaks. In this sense and according to the present stability approach, the VSP cannot be an intrinsic instability, but an extrinsic one.

Let us give some comments on the numerical convergence of the presented results for enough collocation points in both directions. On the one hand, the values of the circular frequencies ω_r are weakly dependent on X_e. On the other hand, the values of the temporal growth rates ω_i are slowly

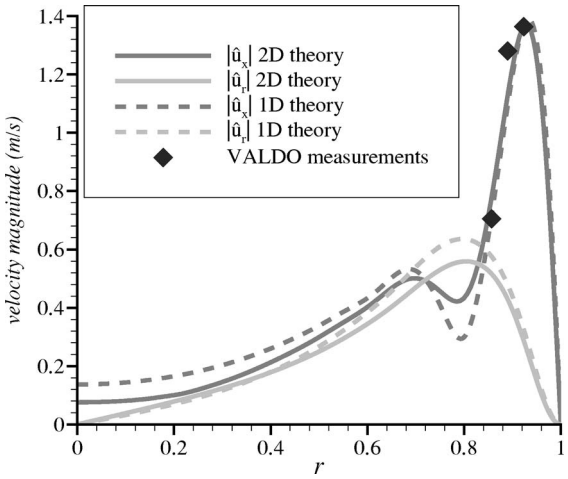

FIG. 10. Radial cut of $|\hat{u}_x|$ and $|\hat{u}_r|$ for the two theories ($x=8.93R=238$ mm, $\omega_r^{1D}=64$, $\omega_r^{2D}=63.576$, $\mathcal{R}e=2100$). The experimental values are plotted as symbols.

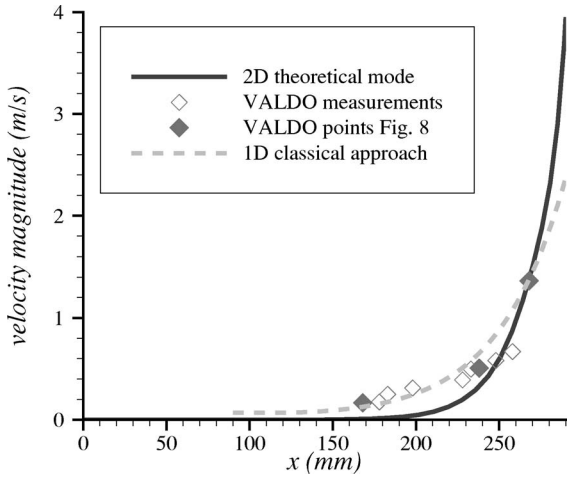

FIG. 11. Comparison of the longitudinal evolution of the rms velocity between the VALDO measurements, the 1D theory, and the 2D approach ($r=0.92R=27.7$ mm, $f=360$ Hz, which corresponds to the 2D mode $\omega_r=63.576$, $V_{inj}=1.05$ m/s, that is, $\mathcal{R}e=2100$). The filled symbols represent the points of Fig. 8 for $r=0.92R$.

increasing with increasing values of X_e. However, they remain always negative. In the following only the values of the frequencies and the sign of the growth rate are taken into account.

Concerning the eigenfunctions, a remarkable characteristic is that the modes behave as progressive 2D waves for large values of x, typically for $x \geqslant 5$. When adding the time dependence $e^{-i\omega t}$ to the perturbation amplitude $\hat{\phi}(x,r)$, waves can be observed which move along the streamlines of the mean flow. This is roughly illustrated by Figs. 9(a) and 9(b). They represent the velocity fields of the mode $\omega_r=63.576$ ($f=360$ Hz) computed with $X_e=10$ and for $\mathcal{R}e=2100$. Two instants are plotted. For the sake of clarity, the velocity fields are drawn artificially using the same size for all the vectors, whereas the rms velocity contours give access to the longitudinal exponential growth of the velocity perturbation field (the darkest, the most amplified). For $8<x<10$ and near $r=1$, one recognizes the typical shape of the parietal vortex shedding (VSP) that has been computed with different Navier-Stokes solvers (see, for instance, Ref. 6). Between the two instances one can see the progression of the wave front that is nearly plane for $x \geqslant 5$. For small values of x, there is a complex organization of the velocity field. It is important to note that in the 1D theory regarding the x direction, the perturbation is searched with a wave dependence expressed by Eq. (6), whereas in the 2D approach the obtained progressive waves are only a consequence of the computation.

For large values of x, the radial shape of the perturbation is expected to be close to that of the 1D theory given that the mean flow is nearly parallel. A radial cut at $x=8.93$ of the longitudinal and radial velocity magnitude is plotted on Fig. 10 for both the 1D and the 2D theories. Both approaches provide eigenmodes with an arbitrary amplitude (linear approach). For comparison, a normalization is required. In Fig. 10, the magnitude of $|\hat{u}_x|$ for both approaches is adjusted in order to match the measured value at $r=0.92$. The radial evolution of the velocities is roughly the same for the two approaches, especially near the injection wall. This result confirms the previous conclusion: the 2D mode behaves like a 1D mode for large values of x. However, this is true for a given frequency. Let us recall that the 1D approach provides a continuous range of frequencies while the 2D approach only provides a discrete set.

Finally, the longitudinal evolution of the perturbations is explored. Figure 11 gives an example at $r=0.92$ for the two approaches in comparison to the available experimental results. The 2D computation is performed for $X_e=10$ and again for $\omega_r=63.576$ and $\mathcal{R}e=2100$. The arbitrary theoretical amplitudes of the 2D and 1D results are chosen in order to coincide with the measuring point $x=8.93$. The axial growth rate is well predicted by the 2D theory, especially for large values of x, whereas the 1D theory gives better results for small values of x. Nevertheless, for small values of x, the rms measured signal for one specific frequency is weak compared to the surrounding noise. As mentioned before, the perturbation exhibits an exponential growth with respect to x for large frequencies ($\omega_r>25$). Thus the present computation has taken into account several orders of magnitude for the perturbation. There is a 10^6 factor between the magnitude of the velocity near $x=0$ and at the exit $X_e=10$.

To summarize the static results, the biglobal stability approach predicts a discrete set of possible frequencies for the eigenmodes. The measured frequencies in VALDO belong to this set. Since all the eigenmodes are temporally damped, a continuous external excitation (added to the exponential growth in x) may explain the fact that some of these modes emerge from the surrounding noise. (It is also possible that a transient growth is responsible of this merging. However, the authors believe, because of the following results, that coupling mechanisms play a major role in the merging of the biglobal modes. Further research will hopefully give more information on this point.)

TABLE III. Range of values of R, V_{inj}, and $\mathcal{R}e$ for the two considered setups.

	Setup	
	VALDO	LP9
R (mm)	constant=30	24.4–42.5
V_{inj} (m/s)	0.6–2	2.60–1.77
$\mathcal{R}e$	1200–4000	3750–6375

D. Dynamic analysis

In this part, the effects of time-dependent values of V_{inj} and/or R are analyzed in order to have a better understanding of the frequency paths that arise in motors. The time dependence of V_{inj} and/or R induces of course a time dependence of the Reynolds number $\mathcal{R}e$. As explained before and thanks to the different time scales, the linear stability equation system is assumed to remain valid at each value of the time. Furthermore, as it has been checked[9] for the 1D approach, the stability results are not very sensitive to a change of the Reynolds number if the latter is large enough (greater than 1000). This is also valid for the 2D approach. Thus, the 2D results are computed from one particular relevant Reynolds number.

Table III summarizes the different ranges of values for R, V_{inj}, and $\mathcal{R}e$ in the following explored cases. For the LP9 setup, the measurements start once the pressure is large enough. It means that there is a difference between the value $R=20$ mm at the beginning of the firing (see Fig. 5) and the first value $R=24.4$ mm used for the measurements.

1. Comparisons with VALDO results

In the VALDO facility, only V_{inj} can vary. Figure 12 presents spectrograms (black spots) of the rms velocity fluctuation. Two cases can be distinguished: whether V_{inj} is increasing (case up) on the left-hand side or decreasing (case down) on the right-hand side. In both cases, the calculated modes are plotted as thin lines and draw a network of lines due to the V_{inj} dependence given by relationship (14). The experimental values seem to be organized in agreement with the discrete 2D modes. The most amplified frequency seems to follow the well identified lines of the theoretical network.

However, VALDO results exhibit a little bending for large values of V_{inj}. This bending is not due to a Reynolds effect but may have two possible origins. First, the porous wall of the VALDO setup has not been designed to work for such large values of V_{inj} and this may affect the results. Second, the use of a slide window to perform the FFT transform induces a little shift that may also explain the observed results. Finally, in spite of the weak bending, the measured amplified frequencies are clearly linearly varying with respect to V_{inj}, as expected by the present model.

It is interesting to plot both previous cases in the same figure. This is done in Fig. 13, which presents for a frequency of around 500 Hz the case up in light gray and the case down in dark gray. Of course, as was shown before, the different frequencies belong to the same network but there is hysteresis. It means that the most amplified frequency at a given injection velocity is not intrinsic. This behavior is coherent with the extrinsic nature of the 2D instability results. We think that in this case (no throat, free exit section) the continuous external source of excitation can be the intrinsic instability (Kelvin-Helmholtz type) of the jet flow that develops at the exit of VALDO. The frequencies involved depend on the jet velocity, which is itself related to the injection velocity V_{inj}. Other configurations tested in VALDO equipped with a throat exhibit amplified frequencies that fol-

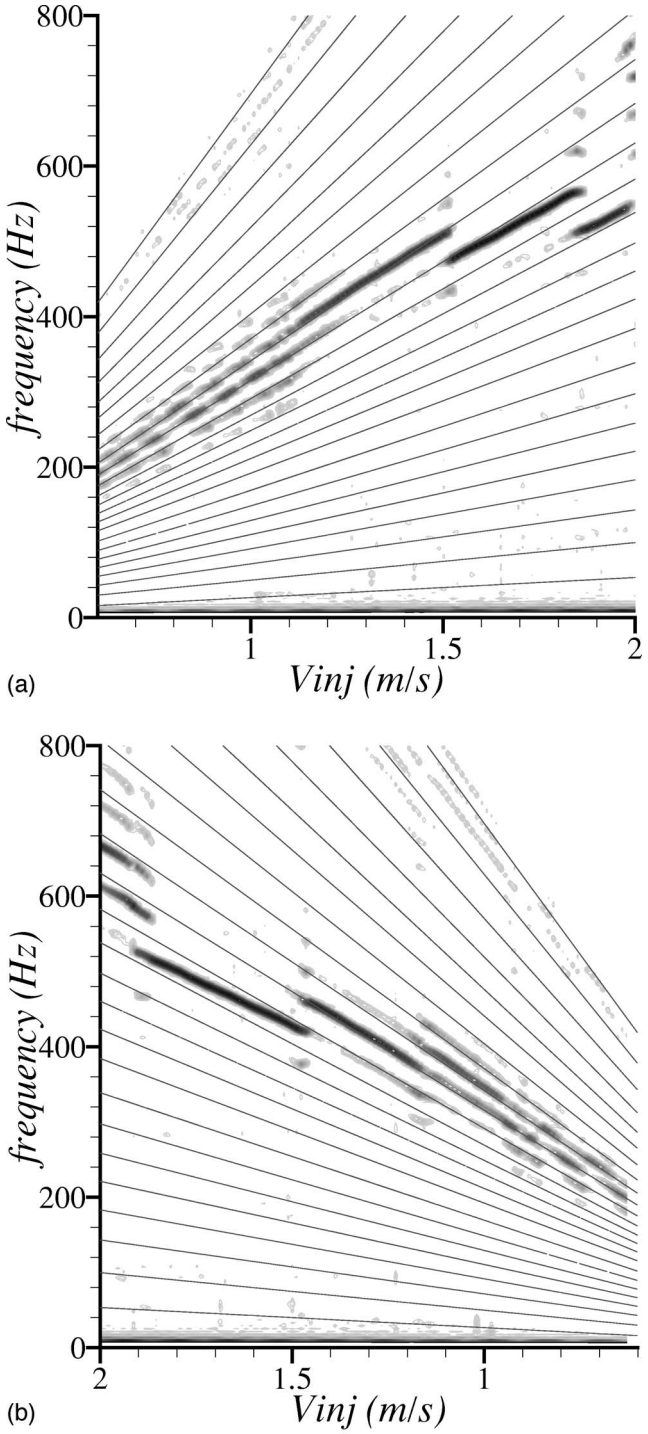

FIG. 12. VALDO frequencies evolution with respect to V_{inj}. The lines correspond to the evolution of the 2D theoretical modes. Case up on the left, case down on the right.

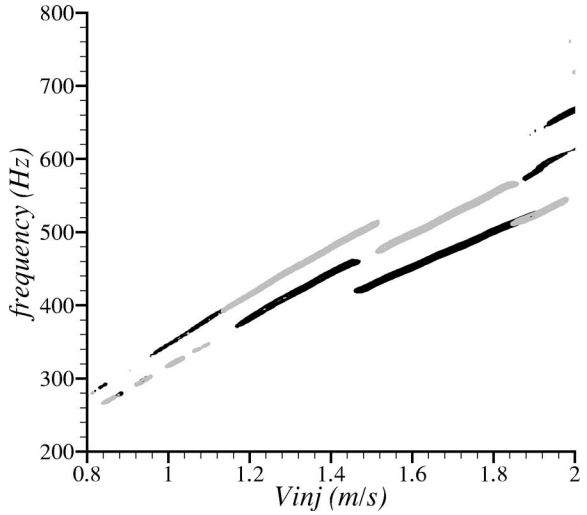

FIG. 13. View of an hysteresis while superimposing the VALDO frequencies evolution for both cases up and down.

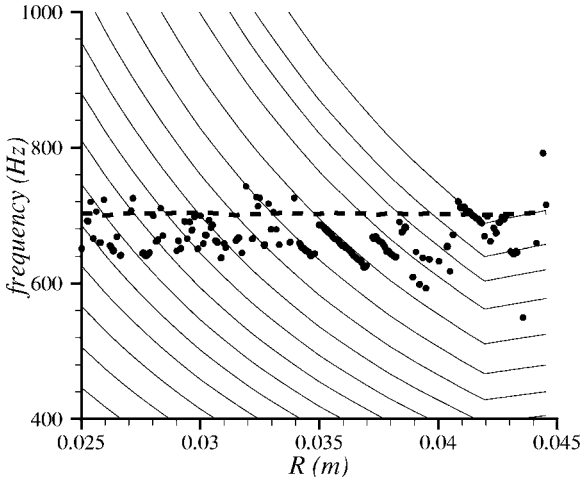

FIG. 14. LP9-15 frequencies evolution with respect to R. The lines correspond to the evolution of the 2D theoretical modes. The first longitudinal acoustic mode is represented as a dashed line.

low once again our theoretical network of 2D modes, but in this case the frequencies associated with the largest amplitudes remain around the fundamental acoustic mode (similarly to live motor experiments). Thus, the external source of excitation is assumed to be the acoustic modes.

2. Comparisons with LP9 results

Here, the "injection" velocity (actually gas velocity at the propellant surface) V_{inj} and the chamber radius R vary during the firing. Thanks to the static pressure signal in the reduced scale motor, it is possible to access the evolution of R and other physical quantities.[37] Moreover, from the unsteady fluctuating pressure signal, a Hilbert transform allows to know the time evolution of the most amplified frequency. As explained in Sec. I (see Fig. 1), this evolution exhibits continuous paths separated by abrupt jumps. At the beginning of the firing, there are no frequency paths and it seems that the most amplified frequency has no particular organization. In those first instances, the ratio R/L, where L stands for the chamber length, is very small. Thus, the flow is expected to become turbulent soon in the streamwise direction. As R increases, the main flow becomes laminar in the major part of the pipe, and this allows the growth of some frequencies. For $t>2.5$ s, the frequency paths appear. They occur around the first acoustic mode of the pipe up to the end of the firing.

The procedure is similar to the one explained in the VALDO case. For an average value of the Reynolds number ($\mathcal{R}e=5000$), the biglobal stability approach is brought into play, leading to a discrete set of ω_r. Then, thanks to (14), the physical frequencies are calculated at each time and are plotted as a network in the same graph of Fig. 1. This is done in Fig 14 with the radius R as an x coordinate instead of the time. At the end of the firing, the propellant is almost fully burned, and the velocity injection has a faster time evolution than the radius R. This explains the particular shape to the 2D mode network at the end.

In spite of the complexity of the physical mechanism that exists in the reduced scale motor LP9, it appears that the observed pressure oscillations follow very well the 2D modes. This confirms the key role of V_{inj}/R in relationship (14) for the observed paths and the discrete nondimensionalized eigenvalues ω_r computed by the biglobal approach. Otherwise, the external source of excitation is clearly the fundamental acoustic mode in the present LP9 case. This is widely confirmed in Ref. 5.

The good agreement given by Fig. 14 is a major result that leads to, as far as we know, a new possible understanding of the thrust oscillations exhibited by large solid rocket motors.

IV. SUMMARY

This paper is devoted to a biglobal stability analysis of a particular unbounded nonparallel steady flow. Taking into account the nonparallel effects on the perturbation form leads to a major modification of the stability results compared to the classical approach. The eigenvalue problem exhibits a discrete spectrum of temporally stable frequencies. A continuous external source of excitation may explain the merging of these stable modes. This sheds light in on the appearance of the pressure oscillations that are observed in reduced scale motors, whether they work with cold gas or with solid propellant. Looking at the results of the different setups, it is clear that the pressure oscillations have a time evolution that is a function of V_{inj}/R. Even if at that time the predicted modes are not fully resolved, it seems that the present 2D approach is able to determine the main amplified frequencies that appear in solid rocket motors. It would also be interesting to make theoretical investigations to understand the complex interaction that may exist between the computational modes and the external source of excitation, for instance, the longitudinal acoustic modes.

TABLE IV. Comparison between the first five eigenvalues given by the ODE-based approach and by the biglobal approach for linearly growing modes.

	N_r, N_r+1	ODE-based approach	Biglobal approach
Mode 1	101, 102	$-0.000\,000\,02-7.989\,816\,73i$	$-0.000\,001\,36-7.989\,816\,41i$
Mode 2	101, 102	$0.819\,404\,69-7.946\,951\,10i$	$0.819\,405\,11-7.946\,953\,56i$
Mode 3	101, 102	$1.585\,774\,34-7.865\,700\,79i$	$1.585\,776\,26-7.865\,702\,15i$
Mode 4	101, 102	$2.338\,485\,24-7.779\,918\,82i$	$2.338\,489\,11-7.779\,921\,16i$
Mode 5	101, 102	$3.069\,852\,16-7.696\,636\,36i$	$3.069\,853\,02-7.696\,635\,17i$
Mode 1	151, 152	$-0.000\,000\,01-7.974\,798\,01i$	$-0.000\,006\,23-7.974\,783\,82i$
Mode 2	151, 152	$0.723\,703\,79-7.944\,533\,15i$	$0.723\,702\,63-7.944\,541\,35i$
Mode 3	151, 152	$1.411\,743\,50-7.882\,614\,27i$	$1.411\,731\,81-7.882\,611\,50i$
Mode 4	151, 152	$2.084\,559\,27-7.814\,919\,52i$	$2.084\,571\,76-7.814\,925\,05i$
Mode 5	151, 152	$2.741\,766\,38-7.747\,904\,56i$	$2.741\,749\,55-7.747\,909\,12i$

ACKNOWLEDGMENTS

This study has been partly supported by the French space agency CNES and partly by ONERA. The authors thank Gérard Avalon from ONERA Palaiseau (VALDO) and Michel Prévost and Jean-Claude Godon from ONERA Fauga (LP9) for their help, valuable comments, and numerous suggestions.

APPENDIX: SYMMETRIC BOUNDARY CONDITION AT THE HEAD END

The Taylor flow can be seen as a symmetric solution with respect to x. At $x=0$, the longitudinal velocity component $U_x^{(b)}$ is zero, whereas the radial velocity component $U_r^{(b)}$ is not. Thus, it seems to be interesting to look at disturbances that satisfy the same set of boundary conditions, in particular at the head end. In that case, it appears that linear solutions with respect to x may exist, as is the case with the well-known Görtler-Hämmerlin modes of the swept attachment line boundary layer.[18] The PDE system (5a) associated to these boundary conditions can be then reduced to a simple ODE system with respect to r. Let $\Psi=xF(r)$ and $\phi=xf(r)e^{-i\omega t}$ be respectively a streamfunction of the Taylor flow and one of the unknown perturbation. Then the system can be written as follows:

$$\frac{1}{r}N(F)L(f)+\frac{1}{r}N(f)L(F)-\frac{F}{r}\frac{dL(f)}{dr}-\frac{f}{r}\frac{dL(F)}{dr}$$

$$=i\omega L(f)f(1)=0,\quad \frac{df}{dr}(1)=0, f(0)=0 \tag{A1}$$

where

$$L=\frac{d}{dr^2}-\frac{1}{r}\frac{d}{dr}$$

and

$$N=\frac{d}{dr}+\frac{2Id}{r}$$

(Id is the identity function). Using a spectral collocation method, it is easy to compute the eigenvalue ω of (A1).

On the other hand, the biglobal approach has been also used to solve the PDE problem. Instead of imposing the no-slip condition, a symmetric condition is applied at $x=0$. It means that the first two conditions of (10) are changed into

$$\frac{\partial^2\hat{\phi}}{\partial x^2}(0,r)=0,\ \hat{\phi}(0,r)=0.$$

Many computations have been done with different values of parameters. For a given number of points in the radial direction N_r, different values of the exit abscissa ($X_e=4$, 5, 6, 8, 10) and of the number of points in the streamwise direction ($N_x=5$, 10, 15, 20) have been tested. Except for spurious modes, all these computations give exactly the same set of eigenvalues (the observed maximum difference is about 0.0001 on the absolute value of an eigenvalue), associated with linearly growing eigenfunctions. The results of the two codes are compared in Table IV for different values of N_r. The first five modes are given in this table. As the eigenvalues are symmetric with respect to the imaginary axis, only the eigenvalues with $\omega_r \geqslant 0$ are written. It is interesting to note that the results in both codes are depend on the parity of N_r. To have access to the whole set of eigenvalues, two computations must be done for N_r and N_r+1.

In the framework of this study, these results do not present a physical interest. There are no experiments, as far as the authors know, that exhibited linear growing modes. For this reason, no details on the structure of the eigenvalue set and on the eigenfunctions will be given here. However, it is a good test case that enables to validate the computational code used for the biglobal approach. Moreover, it proves that the no-slip condition at $x=0$ is necessary to obtain stability results which are in agreement with the experiments.

[1] G. A. Flandro and J. Majdalani, "Aeroacoustic instability in rockets," AIAA J. **41**, 485 (2003).
[2] J. Majdalani and G. A. Flandro, "The oscillatory pipe flow with arbitrary wall injection," Proc. R. Soc. London, Ser. A **458**, 1621 (2002).
[3] J. Majdalani, G. A. Flandro and S. R. Fishbach, "Some rotational corrections to the acoustic energy equation in injection-driven enclosures," Phys. Fluids **17**, 074102 (2005).
[4] F. Vuillot, "Vortex shedding phenomena in solid propellant motors," J. Propul. Power **11**, 626 (1995).
[5] M. Prévost, J. Vetel, F. Plourde, S. Doan-Kim Son, and M. Augelli, "In-

fluence of inhibitor shape in small scale motors and cold-gas set-up," 39th AIAA/ASME/SAE/ASEE Joint Propulsion Conference and Exhibit, Huntsville, USA July 20–23, 2003, AIAA 2003–4673.
[6]N. Lupoglazoff and F. Vuillot, "Parietal vortex shedding as a cause of instability for long solid propellant motors. Numerical simulations and comparisons with firing tests," *34th Aerospace Sciences Meeting and Exhibit*, Reno, AIAA 96-0761 (1996).
[7]V. N. Varapaev and V. I. Yagodkin, "Flow stability in a channel with porous wall," Izv. Akad. Nauk SSSR, Mekh. Zhidk. Gaza **4**, 91 (1969).
[8]J. Griffond and G. Casalis, "On the dependence on the formulation of some nonparallel stability approaches applied to the Taylor flow," Phys. Fluids **12**, 466 (2000).
[9]G. Casalis, G. Avalon, and J. Ph. Pineau, "Atial instability of planar channel flow with fluid injection through porous walls," Phys. Fluids **10**, 2558 (1998).
[10]J. Griffond, G. Casalis, and J. Ph. Pineau, "Spatial instability of flow in a semiinfinite cylinder with fluid injection through its porous walls," Eur. J. Mech. B/Fluids **19**, 69 (2000).
[11]R. S. Brown, R. Dunlap, S. W. Young, and R. C. Waugh, "Vortex shedding as a source of acoustic energy in segmented solid rockets," J. Spacecr. Rockets **18**, 312 (1981).
[12]T. Tatsumi and T. Yoshimura, "Stability of the laminar flow in a rectangular duct," J. Fluid Mech. **212**, 437 (1990).
[13]V. Theofilis, "Linear instability analysis in two spatial dimensions," *Fourth ECCOMAS Computational Fluid Dynamics Conference*, ECCOMAS98, Athens (1998).
[14]V. Theofilis, P. W. Duck, and J. Owen, "Viscous linear stability analysis of rectangular duct and cavity flows," J. Fluid Mech. **505**, 249 (2004).
[15]J. Ch. Robinet and P. de la Motte, "Global instabilities in separated boundary layers," Third International Symposium on Turbulence and Shear Flow Phenomenon (TSFP-3), Sendai, Japan (2003).
[16]R. S. Lin and M. Malik, "On the stability of attachment-line boundary layers. Part 1. The incompressible swept Hiemenz flow," J. Fluid Mech. **311**, 239 (1996).
[17]V. Theofilis, S. Hein and U. Dallmann, "On the origins of unsteadiness and three-dimensionality in a laminar separation bubble," Philos. Trans. R. Soc. London **358**, 3229 (2000).
[18]V. Theofilis, A. Fedorov, D. Obrist, and U. Ch. Dallmann, "The extended Görtler-Hämmerlin model for linear instability of three-dimensional incompressible swept attachment-line boundary layer flow," J. Fluid Mech. **487**, 271 (2003).
[19]C. Robitaillié-Montané, Th. Féraille, and G. Casalis, "Linear stability of the incompressible swept Hiemnez flow : A 2D model," in *21st International Congress of Theoretical and Applied Mechanics*, Warsaw (2003).
[20]A. Berman, "Laminar flow in channels with porous walls," J. Appl. Phys. **24**, 1232 (1953).
[21]P. Huerre and M. Rossi, *Hydrodynamic Instabilities in Open Flows* (Cambridge University Press, Cambridge, 1998).
[22]M. B. Zaturska, P. G. Drazin, and W. H. H. Banks, "On the flow of a viscous fluid driven along a channel by suction at porous walls," in *Fluid Dynamics Research 4* (North-Holland, Amsterdam, 1988), pp. 151–178.
[23]S. Ferro and G. Gnavi, "Spatial instability of similarity solutions for viscous flows in channels with porous walls," Phys. Fluids **12**, 797 (2000).
[24]G. Casalis and F. Vuillot, "Motor flow instabilities—Part 2 : Intrinsic linear stability of the flow induced by wall injection," RTO-AVT VKI Special Course on Internal Aerodynamics in Solid Rocket Propulsion (2002).
[25]R. Dunlap, A. M. Blackner, R. C. Waugh, R. S. Brown, and P. G. Willoughby, "Internal flow field studies in a simulated cylindrical port rocket chamber," J. Propul. Power **6**, 690 (1990).
[26]J. Barron, W. Van Moorhem, and J. Majdalani, "A novel investigation of the oscillatory field over a transpiring surface," J. Sound Vib. **235**, 281 (2000).
[27]G. Avalon and D. Lambert, Campagne d'essais VALDO, période 2000/2001, ONERA, Etablissement de Palaiseau RT 2/05424 DEFA (2001).
[28]J. C. Godon and M. Prévost, "Restitutions et analyses des instabilités des essais no 10 à 15 du montage LP9—démonstrateur de VSP, ONERA, Etablissement du Fauga-Mauzac RT 2/08692 DEFA/DMAE, CNES-RT-NT-1331-0402-ONERA-01 (2004).
[29]V. Yang, "Overview of motor internal flow dynamics," RTO-AVT VKI Special Course on Internal Aerodynamics in Solid Rocket Propulsion (2002).
[30]W. W. Chu, V. Yang, and J. Majdalani, "Premixed flame response to acoustic waves in a porous-walled chamber with surface mass injection," Combust. Flame **133**, 359 (2003).
[31]A. B. Vyas, J. Majdalani, and V. Yang, "Estimation of the laminar premixed flame temperature and velocity in injection-driven combustion chambers," Combust. Flame **133**, 371 (2003).
[32]J. Griffond and G. Casalis, "Linear stability of injection induced flow: Effect of weak unsteadiness," *International Conference on Stability and Turbulence*, Novosibirsk (1999).
[33]C. Canuto, M. Y. Hussaini, A. Quarteroni, and T. A. Zan, *Spectral Methods in Fluid Dynamics* (Springer, New York, 1987).
[34]W. S. Edwards, L. S. Tuckerman, R. A. Friesner, and D. C. Sorensen, "Krylov methods for the incompressible Navier-Stokes equations," J. Comput. Phys. **110**, 82 (1994).
[35]V. Theofilis, "Advances in global linear instability analysis of nonparallel and three-dimensional flows," Prog. Aerosp. Sci. **39**, 249 (2003).
[36]B. Ugurtas, "Etude numérique et expérimentale des instabilités hydrodynamiques et du couplage aéro-acoustique dans unécoulement de Taylor," Ph.D. thesis Université Paris VI (2000).
[37]J-Cl. Godon, "Code PERSE: Une approche unidimensionnelle dans la modélisation du fonctionnement stationnaire d'un propulseurà propergol solide," 3ème colloque R&D "Ecoulements internes en propulsion solide," Poitiers (1998).